3 Coarse-Graining Parameterization and Multiscale Simulation of Hierarchical Systems. Part II: Case Studies

Steve Cranford and Markus J. Buehler

CONTENTS

3.1 INTRODUCTION

To illustrate the coarse-grain parameterization and multiscale methodology, we provide a more thorough discussion regarding the development of specific mesoscopic models. The focus is on the coarse-grain potential development, to provide examples of the model formulation framework described in depth in Chapter 2. It is noted that some equations are repeated to provide a self-contained and complete description of each model formulation within each case.

The three chosen case studies are presented to exemplify both the finer-trains-coarser multiscale paradigm (that is, use of full atomistic test suites to parameterize the coarse-grain potentials), as well as a system-dependent approach (the developed coarse-grain potentials are unique to the intended application) as previously discussed. Our intent is to differentiate general coarse-graining frameworks [such as the aforementioned elastic network model (ENM) or MARTINI force field] from system-specific coarse-graining development. The merits of either approach, of course, are both subjective and problem-specific and judicious consideration of the resulting simulation design and intent is required.

For a broader perspective, each case study presented represents a fundamental advantage to all coarse-graining approaches, and thus can be considered as archetype coarse-graining problems. Sections 3.1.1 through 3.1.3 discuss characteristics of the case studies presented in this chapter.

3.1.1 Investigate the Structure–Property Relation at the Mesoscale

A primary motivation for the development of a coarse-grain representation is to provide a means to directly model system behavior at the mesoscopic scale. With the coarse-grained representation, structures approaching micrometers in scale can be efficiently modeled. Because of the use of a finer-trains-coarser approach, the atomistic behavior and intramolecular interactions are maintained, thereby providing a necessary intermediate step reconciling the gap between atomistic and continuum theory. Here, we specifically wish to investigate two materials, carbon nanotubes and collagen, that form hierarchical secondary structures at length scales beyond the capacity of full atomistic representation, but yet are dependent on intermolecular adhesion and interaction. These secondary structures (nanotube arrays and collagen fibrils) have unique structural arrangements that directly affect the mechanical properties. Thus, neither an atomistic chemical description nor continuum material properties are sufficient to describe the structure-property relation at the mesoscale. It is intended that the coarse-grain representation can be used to investigate such behavior. The coarse-grain models we present provide a method to model and investigate this class of nanostructures that fall precariously between atomistic and continuum techniques.

3.1.2 Extend Atomistic Behavior to Inaccessible Time- and Length-Scales

A fundamental limitation of full atomistic molecular dynamics simulations is the accessible (or inaccessible) time and length scales. As a consequence, it is frequently difficult to extend theoretically well-described atomistic behavior to physically relevant time and length regimes. By integrating atomistic behavior into developed coarse-grain potentials, larger systems can be simulated for longer time spans, while representing complex molecular interactions and properties. Precise definition of the intended behavior is required to develop accurate coarse-grain representation. Case Study II presents the development of a coarse-grain model to represent the unfolding behavior of alpha-helical protein domains. The unfolding behavior is initiated by the rupture of hydrogen bonds—an unquestionable atomistic response—and is supported by full atomistic simulations. Coarse-graining is introduced here to both examine the length dependencies of this unfolding response and investigate such proteins in networked systems (as found in biological cells and membranes).

3.1.3 Minimize Degrees of Freedom for Large Systems

Simulations of molecular systems in solution are often hindered by the computational overhead of calculation of the reactions of water molecules, regardless of the interaction with the relevant macromolecule. Indeed, the degrees of freedom associated with the solvent can exceed the macromolecule by an order of magnitude or more. By design, parameterization of coarse-grain potentials fully integrates the effects of water molecules, eliminating the need for either explicit water molecule representations or applied implicit water force fields. Case Study III illustrates the coarse-graining of polymer-tethered fullerenes to allow the investigation of self-association of such large nanoparticles in solution and efficient investigation of the effects of parameters such as molecular weight, polymer architecture, and particle density.

There is significant overlap for all presented case studies in the sense that each investigates the structure–property relationship, extends the accessible time and length scales, and reduces the number of degrees of freedom. However, each is differentiated by the associated advantage for coarse-graining, and the approach for each system subsequently differs based on intent and utilization of the model. Relevant applications for each model are described to provide an understanding of the intentions and benefits of the coarse-grain representation. The discussion of applications is relatively brief, to emphasize model development and intent rather than results of specific investigations. The reader is encouraged to refer to the cited literature for each case study for more details.

3.2 CASE STUDY I: CARBON NANOTUBES AND TROPOCOLLAGEN

At the atomistic scale, carbon nanotubes (CNTs) [1,2] and collagen differ in terms of structure and behavior. Carbon nanotubes consist of rolled sheets of graphene (single-layer bonded carbon), which form rigid cylindrical structures with high aspect ratios (Figure 3.1a). Carbon nanotubes are among the most widely studied

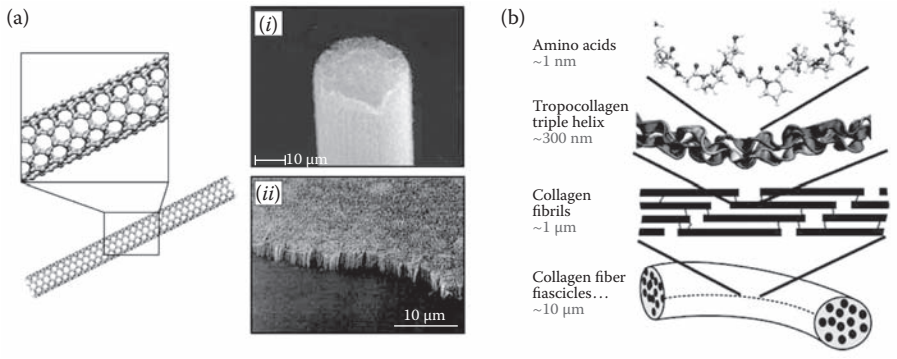

FIGURE 3.1 **(See color insert following page 146.)** Overview of carbon nanotube and tropocollagen systems. (a) Depiction of full atomistic representation of (5,5) carbon nanotube. Subplots show higher order hierarchical arrangements, including (i) SEM of single bundle of carbon nanotubes (Reprinted in part with permission from McClain, D., et al., *J. Phys. Chem. C*, 111(20), 7514–7520, 2007. Copyright 2007 American Chemistry Society.) and (ii) SEM micrograph of vertically aligned carbon nanotube array (Reprinted in part with permission from Yang, J. and Dai, L., *J. Phys. Chem. B*, 107, 12387–12390, 2003. Copyright 2003 American Chemical Society.). (b) Schematic view of some of the hierarchical features of collagen, ranging from the amino acid sequence level at nanoscale up to the scale of collagen fibers with lengths on the order of 10 μm. (From Buehler, M.J., Keten, S., and Ackbarow, T., *Prog. Mater. Sci.,* 53, 1101–1241, 2008.) The coarse-grain model development discussed here is focused on the behavior of tropocollagen molecules (component level) and their role in the mechanical behavior and properties of collagen fibrils (system level).

nanomaterials, with many potential applications that take advantage of their unique mechanical, electrical, thermal, and optical properties [6]. There are many concurrent investigations involving carbon nanotubes, ranging from experimental synthesis to atomistic and continuum modeling with a focus on a variety of properties, behaviors, and applications. The superior mechanical properties of carbon nanotubes are appealing for their potential use in novel nanomaterials. For instance, the Young's modulus of a single-walled nanotube approaches a terapascal (10^{12} Pa) [7], implying one of the strongest known synthesized materials in terms of elastic modulus and ultimate tensile strength [8]. Collagen, in contrast, is a protein-based material, composed of polypeptide chains of various constituent amino acids (Figure 3.1b). A tropocollagen molecule is composed of three polypeptide chains arrange in a helical structure, stabilized by hydrogen bonding between different residues [3–5,9]. The Young's modulus of tropocollagen is on the order of 4 to 10 GPa [3, 10–12]. Materials based on proteins hold particular promise because of their great flexibility in usage and their applications and the potential integration of technology and biology, allowing translation of nature's structural concepts into engineered materials [13].

The motivating factor for the coarse-graining of both carbon nanotubes and collagen fibrils (and fibers) is the investigation of the materials at the mesoscopic hierarchical level. For carbon nanotubes, a well-known behavior is intertube bonding due to weak van der Waals interactions, which results in the formation of bundles that contain hundreds or thousands of individual nanotubes (Figure 3.1a, inset). At

the microscale, collagen fibrils consisting of staggered, crosslinked tropocollagen molecules form the basis for biological tissues such as tendon and bone. The formation of these mesoscopic structures complicates the full atomistic investigation of the mechanical properties. However, due to the homogeneous and fibrillar structure of both carbon nanotubes and tropocollagen, the formulation of their respective coarse-grain models is the same.

3.2.1 Model Development

The coarse-grain model developed is intended to capture two essential components of both carbon nanotubes and tropocollagen: (1) the mechanical behavior of the fibrillar structure for both stretching and bending and (2) the intermolecular interactions between adjacent macromolecules. The intent is to apply a coarse-graining approach to achieve a mechanical response while maintaining atomistic interactions, an approach more apropos than equivalent continuum or elasticity techniques due to the system dependence on intermolecular interactions. We thus define the energy landscape as

$$E_{CG} = E_{bond} + E_{angle} + E_{pair} \tag{3.1}$$

To obtain the necessary parameters for these potentials, the atomistic behavior of each must be investigated and full atomistic molecular dynamics simulations are undertaken to determine key mechanical property values.

For the current fibrillar structures, the coarse-grain bond potential, E_{bond}, is representative of axial strain. Furthermore, the intended coarse-grain application is limited to tensile stretching. Thus, a simple simulation is developed to determine the force-displacement or stress-strain relationship of the macromolecule. We apply tensile deformation by keeping one end of the molecule fixed and slowly displacing the other end in the axial direction (Figure 3.2a). In terms of mechanical properties, this relationship can be converted to Young's modulus, E. It is noted that the atomistic behavior is not meant to correspond one-to-one with continuum properties such as Young's modulus, which is typically limited to an elastic isotropic material, but such properties provide appropriate, conventional, and convenient measures for behavior such as axial stretching.

From the full atomistic results (Figure 3.3), the axial stretching behavior of both carbon nanotubes and tropocollagen consists of two regimes. For carbon nanotubes, there is nonlinear softening and plastic deformation due to the yielding of carbon bonds, whereas tropocollagen undergoes nonlinear stiffening due to the extension and unfolding of the helical arrangement and transition to direct straining of the protein backbone. Both carbon nanotubes and tropocollagen fracture at an ultimate strain. Although the nonlinear behavior is the result of complex atomic interactions, it is a trivial simplification to integrate the desired effect into the coarse-grain potential. We can determine Young's modulus either directly from stress-strain results, or indirectly via force-displacement results, depending on the output and sophistication of the full atomistic simulation, where

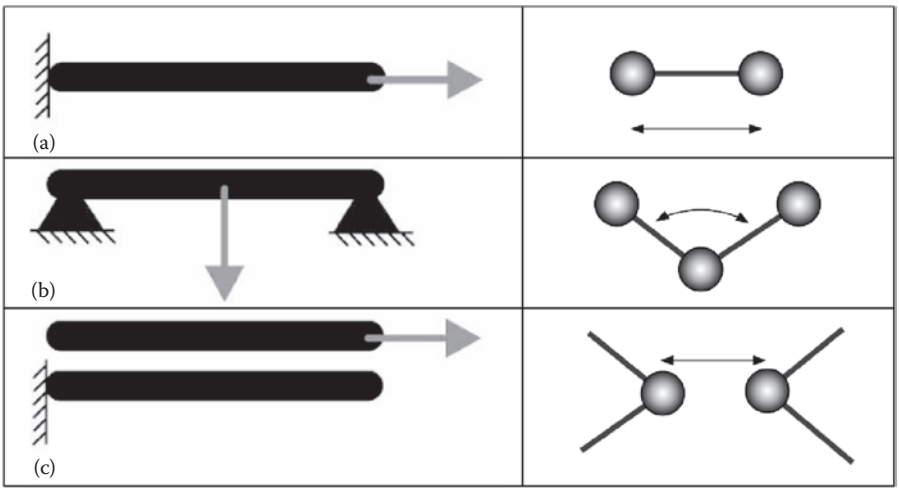

FIGURE 3.2 Atomistic "test suite" and corresponding coarse-grain potential behavior: (a) axial stretching, bond potential; (b) three-point bending, angle potential; (c) surface adhesion; pair potential.

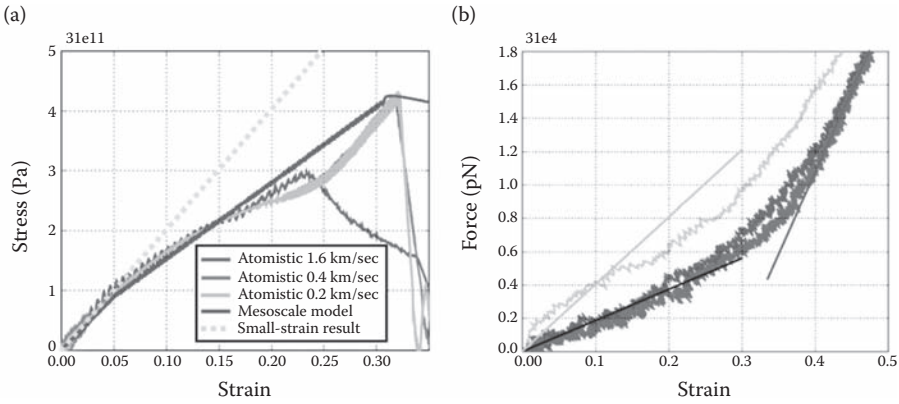

FIGURE 3.3 **(See color insert following page 146.)** Full atomistic simulation results for the axial stretching of (a) a single-walled carbon nanotube (From Buehler, M.J., *J. Mater. Res.* 21(11), 2855–2869, 2006. With permission.) and (b) a tropocollagen molecule (From Buehler, M.J., *J. Mater. Res.*, 21(8), 1947–1961, 2006. With permission.). The nanotube results depict a softening behavior as the carbon bonds yield at high strain, while the tropocollagen results depict a stiffening behavior, as the molecule undergoes extension of the helical structure before direct straining of the protein backbone.

$$E = \frac{\partial \sigma}{\partial \varepsilon} \approx \frac{\Delta \sigma}{\Delta \varepsilon} = \frac{r_0}{A_c} \frac{\Delta F}{\Delta r} \tag{3.2}$$

where σ and ε are the stress and strain, F and r are the force and displacement, and A_c and r_0 are the cross-sectional area (assumed constant) and initial length. For small deformation (initial stretching regime), the Young's modulus for a (5,5) single-walled carbon nanotube was calculated to be approximately 2 TPa, while the modulus for tropocollagen was determined to be on the order of 8 GPa. For nonlinear behavior, the Young's modulus is calculated for each regime independently. The total bond energy of the coarse-grain system is given by the sum over all bonded interactions or:

$$E_{\text{bond}} = \sum_{\text{bonds}} \phi_t(r) \tag{3.3}$$

For axial stretching, a simple harmonic spring is used to determine the energy between all bonded pairs of particles in the system, given by

$$\phi_t(\Delta r) = \frac{1}{2} k_t \left(r - r_0\right)^2 = \frac{1}{2} k_t \Delta r^2, \tag{3.4}$$

with k_t as the spring constant relating distance, r, between two particles relative to the equilibrium distance, r_0. We assume each linear regime can be approximated using the equivalent elastic strain energy,

$$U(\varepsilon) = \frac{1}{2} \int_{\bar{V}} (\sigma \varepsilon) \, \mathrm{d}\bar{V} = \frac{1}{2} \frac{A_c E \Delta r^2}{r_0} = U(\Delta r) \tag{3.5}$$

For the integration over the volume, $\bar{V}$, we assume a constant cross-section, A_c, such that $\bar{V} = A_c r_0$, define strain, $\varepsilon = \Delta r / r_0$, and stress, $\sigma = E\varepsilon$. We note that we utilized the full atomistic simulations to determine Young's modulus specifically to allow this formulation of strain energy in our parameterization. Caution must be taken not to overextend the significance of the atomistic to continuum equivalence. Here, we only apply Young's modulus to characterize the work required to stretch our atomistic model and thus train the coarse-grain potential. It is not implied that either carbon nanotubes or tropocollagen can be suitably modeled by elastic formulations. Indeed, unlike the Young's modulus of elastic isotropic materials, the modulus determined by atomistic simulation can differ depending on system properties, atomistic force field, boundary conditions, and loading rates (see Buehler [3,4], for example). For equivalent energy and consistent mechanical behavior, we let $\phi_t(\Delta r) = U(\Delta r)$ and find

$$k_t = \frac{A_c E}{r_0} \tag{3.6}$$

To account for the nonlinear stress-strain behavior under tensile loading, a bilinear model that has been used successfully in previous studies [15,16] is applied where:

$$\phi_t(r) = H\left(r_{\text{fracture}} - r\right)\begin{cases} \frac{1}{2}k_t^0\left(r - r_0\right)^2, & r < r_1 \\ \beta(r) + \frac{1}{2}k_t^1\left(r - r_1\right)^2, & r \geq r_1 \end{cases}, \tag{3.7}$$

where $H(r_{\text{fracture}} - r)$ is the Heaviside function $H(a)$, which is defined to be 0 for $a < 0$ and 1 for $a \geq 0$, k_t^0 and k_t^1 are the spring constants for the different deformation regimes, and $\beta(r)$ is obtained from continuity conditions where:

$$\beta(r) = \frac{1}{2}k_t^0\left(r_1 - r_0\right)^2 + k_t^0\left(r_1 - r_0\right)\left(r - r_1\right) \tag{3.8}$$

A schematic of the resulting force-displacement relationship is shown in Figure 3.4. The same technique can be extended to multiple linear regimes, maintaining a computationally inexpensive harmonic potential while incorporating nonlinear effects.

For the angle potential, E_{angle}, the bending stiffness and force-displacement behavior of each structure is required. A simple three-point bending test is simulated via full atomistic representation, with the macromolecule subjected to bending by a center point load (Figure 3.2b). From the results, we can determine the bending stiffness

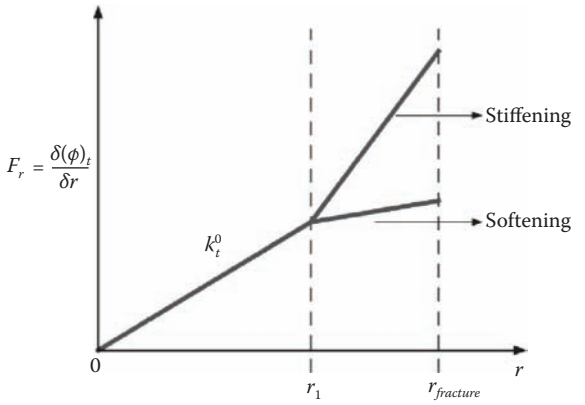

FIGURE 3.4 Plot of bilinear force model to account for nonlinear stiffening (collagen) or softening (carbon nanotubes) and fracture, as described by the potential in Equation 3.24.

of the molecule, which we label *EI*, using continuum beam theory to describe the mechanics of our system:

$$EI = \frac{L^3}{48}\left(\frac{F}{d}\right), \tag{3.9}$$

where L is the bent length of the molecule, F is the applied load at the center of the span, and d is the maximum displacement (at the load point). Application of beam-theory to atomistic simulations is a matter of judgment, as considerations must be made for deformation mechanisms (i.e., the presence of nonlinear plastic hinging or shear deformation). Furthermore, it is again stressed that the continuum interpretation of *EI*, the product of Young's modulus and area moment of inertia, is not applicable to all atomistic simulations. Here we use *EI* as a convention to characterize the bending stiffness of the molecule and assist in the formulation of the coarse-grain potential. However, for a rigid molecule such as a carbon nanotube, a continuum approximation can provide support to help validate resultant simulation values. Indeed, for the (5,5) single-walled carbon nanotube, full atomistic simulated bending results in a bending stiffness, *EI*, of 6.65×10^{-26} N-m^2. Using the previously determined E of 2 TPa, with a conservative approximation of I (assuming a solid cylinder with diameter 6.8 Å), we calculate a bending stiffness, $EI_{\text{theoretical}}$, of 2.1×10^{-26} N/m^2, which is on the same order of magnitude as the atomistic results. The bending energy is given by a sum over all triples in the system, given by

$$E_{\text{angle}} = \sum_{\text{triples}} \phi_\theta(\theta) \tag{3.10}$$

For bending, a rotational harmonic spring potential is used to determine the energy between all triples of particles in the system:

$$\phi_\theta(\theta) = \frac{1}{2} k_\theta \left(\theta - \theta_0\right)^2, \tag{3.11}$$

with k_θ as the spring constant relating bending angle, θ, between three particles relative to the equilibrium angle, $\theta_0 = 180°$. Using the equivalent elastic energy [17],

$$U(d) = \frac{48EI}{\left(2r_0\right)^3} d^2 \tag{3.12}$$

For small deformation, $\theta - \theta_0 \approx 2d/r_0$, and letting $\phi_\theta(d) = U(d)$:

$$k_\theta = \frac{3EI}{r_0} \tag{3.13}$$

We next characterize weak interactions (van der Waals interactions) between all pairs of coarse-grain elements, E_{pair}. The weak interactions represent the adhesion between adjacent macromolecules, thus a full atomistic simulation with two molecules (usually copies of the original) is simulated to determine the adhesion energy (Figure 3.2c). The energy barrier and equilibrium distance can be quickly determined by minimizing the atomistic system at two distinct states: (1) when the molecules are in contact energy minimum and (2) when the molecules are arbitrarily separated such that the interaction is negligible (the required separation is dependent on the relative adhesion strength of the simulated system). Differences in energy minima can be used to extract potential energy gain of adhesion (E_{adhesion}), while the geometric configuration at contact can be used to determine equilibrium distances (D_{adhesion}). A more sophisticated approach would be to determine the potential energy as a function of separation for a more accurate fitting of the coarse-grain potential. However, here we assume a LJ 12:6 function to represent adhesion, requiring only the potential energy well depth and equilibrium spacing for parameterization.

For the current bead-spring representation, we require the adhesion energy per unit length. From the atomistic simulation results, with an adhesion energy gain, E_{adhesion}, and a total molecular contact length, L, we define the adhesion energy per unit length, E_{L}, as

$$E_{\text{L}} = \frac{1}{2}\frac{E_{\text{adhesion}}}{L} \tag{3.14}$$

The total adhesion energy of the coarse-grain system is given by the sum over all pairs or

$$E_{\text{pairs}} = \sum_{\text{pairs}} \phi_{\text{LJ}}(r) \tag{3.15}$$

We use the LJ 12:6 function for each pair interaction:

$$\phi_{\text{LJ}}(r) = 4\varepsilon\left[\left(\frac{\sigma}{r}\right)^{12} - \left(\frac{\sigma}{r}\right)^{6}\right], \tag{3.16}$$

where ε describes the energy well depth at equilibrium, and σ is the distance parameter. We assume that a pair-wise interaction between different particles is sufficient to describe the adhesion between the coarse-grain elements, and that there are no multibody considerations. For both carbon nanotubes and tropocollagen, this assumption is deemed appropriate. As the coarse-grain particles are fundamentally point masses, we must assign a representative thickness to our representation via the pair potential. For the carbon nanotube, this is representative of the diameter of the tube. For a molecule such as tropocollagen, a thickness is approximated based on the molecular cross-section and assumed boundaries of atomistic interaction. We can then determine the distance parameter for the LJ function:

$$\sigma = \frac{D_{\text{adhesion}} + t}{\sqrt[6]{2}}, \tag{3.17}$$

where D_{adhesion} is the equilibrium distance between macromolecules determined via atomistic simulation, and t is the representative thickness. To illustrate, the equilibrium distance between two (5,5) single-walled carbon nanotubes was determined to be 3.70 Å, and each tube has a diameter of approximately 6.8 Å. Using the Equation 3.17, we find $\sigma \approx 9.35$ Å. Note that the equilibrium spacing between coarse-grain particles is now approximately 10.5 Å, on the order of the bead-spring bond length. Choice of bond length, r_0, and choice of thickness, t, are critical parameters determining bead-bead interactions, and a balance may be required if intermolecular adhesion is a pertinent system behavior (Figure 3.5).

If the bond length is much greater than the equilibrium distance of the pair potential, $r_0 >> r_{\text{LJ}}$, it is possible for coarse-grain molecules to be in close contact, or even pass through each other under certain conditions. If the bond length is relatively large, $r_0 > r_{\text{LJ}}$, the energy landscape about the equilibrium conformations is not smooth and can result in a "stick-slip" mechanism for molecules in contact as particles pass from neighbor to neighbor. Further, if the bond length is relatively short in comparison to equilibrium separation, $r_0 < r_{\text{LJ}}$, configurations may occur where a particle is in equilibrium with its second-nearest neighbors, while being repelled by the closest molecular surface. All arrangements of bond distance maintain energy equivalence between atomistic and coarse-grain potentials, but do not result in consistent mechanical behavior. In general, the bond length is chosen around the pair potential equilibrium distance, to ensure consistent mechanical behavior and a smooth energy landscape. For carbon nanotubes, we choose an equilibrium bead-spacing, r_0, of 10 Å ($r_{\text{LJ}} = 10.5$ Å), while for tropocollagen, we choose a bead-spacing of 14 Å ($r_{\text{LJ}} = 16.5$ Å).

The potential minimum, represented by the adhesion energy per unit length, E_{L}, is given by ε for the LJ 12:6 function. This parameter in the coarse-grain model is chosen such that the interaction of a single pair of beads is the same as the adhesion energy for the representative length of the full atomistic model. For nearest neighbors only, we find:

$$\varepsilon = E_{\text{L}} r_0 \tag{3.18}$$

To account for the interactions of next-nearest neighbors in the energy contribution to the atomistic results, we note, at equilibrium:

$$E_{\text{L}} r_0 = \phi^{(1)}(r_{\text{LJ}}) + \phi^{(2)}(r_2) + \phi^{(3)}(r_3) + \ldots + \phi^{(n)}(r_n) \tag{3.19}$$

Or, the total adhesion energy along the coarse-grain element length is the summation of the nearest-neighbor interactions, and "n" next-nearest neighbor interactions, $\phi^{(n)}(r_n)$, at distances r_n. Thus, for more than one nearest neighbor,

$$\varepsilon = E_{\text{L}} r_0 \left[\left(1 + \pi^{(2)} + \pi^{(3)} + \ldots + \pi^{(n)} \right)^{-1} \right], \tag{3.20}$$

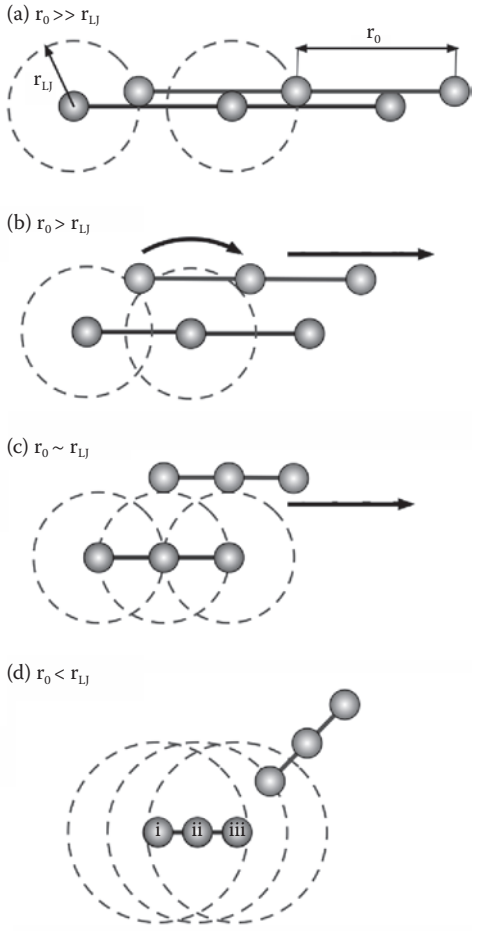

FIGURE 3.5 Energy landscape as a result of the relative magnitudes of bond distance, r_0, and pair potential equilibrium distance, r_{LJ}. (a) $r_0 >> r_{LJ}$, potentially resulting in false equilibrium configurations, or allowing the passing of particles through bonds; (b) $r_0 > r_{LJ}$, rough energy landscape resulting in a "stick-slip" mechanism for adjacent molecules; (c) $r_0 \sim r_{LJ}$, best practice for consistent mechanical behavior and smooth energy landscape; (d) $r_0 < r_{LJ}$, potential equilibrium with next-nearest neighbor, particle (ii) while being repelled by nearest neighbor, particle (iii), yet attracted to third-nearest neighbor, particle (i), resulting in inconsistent mechanical behavior.

where $\pi^{(i)} = \phi^{(1)}(r_{LJ})/\phi^{(i)}(r_i)$. We define the term $(1 + \pi^{(2)} + \pi^{(3)} + \ldots + \pi^{(n)}) = \beta^{(n)}$, and then the above equation reduces to

$$\varepsilon = \frac{E_L r_0}{\beta^{(n)}}, \tag{3.21}$$

where $\beta^{(n)}$ is a numerical factor to account for next-nearest neighbor interactions. The calculation $\beta^{(n)}$ depends on the geometry of the coarse-grain system, as well as

consideration for the cutoff of the pair potential (which dictates the extent of considered neighbors). For the current model of bead-springs for carbon nanotubes and tropocollagen, we use the first six nearest neighbors, and find $\beta^{(6)} \cong 1.1$. The factor, $\beta^{(n)}$, thus represents a reduction in the energy well depth of individual pairs, as the full atomistic representation implicitly accounts for the interaction with next-nearest neighbors.

The final consideration for the mesoscopic coarse-grain model is the assignment of mass to the particles. The mass of each bead is determined by assuming a homogeneous distribution of mass in the molecular model. Given the homogeneous structure of CNTs and tropocollagen, this is a reasonable approximation. The mass of each bead will scale with the selection of equilibrium bond distance, r_0, as each bead is representative of a larger portion of the full atomistic model. It behooves us to note that the full implication of this mass assignment approach to coarse-grain models on such thermodynamic properties as temperature effects has not been thoroughly investigated. However, the approach has proven adequate for investigations focusing on mechanical behavior at constant temperature conditions.

Finally, we can now define the mesoscopic model potentials by six parameters: k_t, r_0, k_θ, θ_0, σ, and ε. The results from the described atomistic simulations are used to determine these six parameters via equilibrium conditions (r_0, θ_0, σ) and energy conservation (k_t, k_θ, ε) by imposing energy equivalence and consistent mechanical behavior. The parameters can be extended to represent nonlinear effects, as illustrated by the bilinear function implemented for the softening or stiffening of the carbon nanotube or tropocollagen respectively. As such, the parameter k_t can be thought of as a set of parameters, depending on the complexity of the developed potential. All parameters of the coarse-grain potentials developed for a (5,5) SWCNT and a tropocollagen molecule are given in Table 3.1, derived completely from the results of full

TABLE 3.1
Summary of Coarse-Grain Parameters for the Bond, Angle, and Pair Potentials of a (5,5) SWCNT and a Tropocollagen Molecule

Parameter	SWCNT	Tropocollagen
Equilibrium bead distance, r_0 (Å)	10.00	14.00
Tensile stiffness parameter, k_t^0 (kcal/mol/Å^2)	1000.00	17.13
Tensile stiffness parameter, k_t^1 (kcal/mol/Å^2)	700.00	97.66
Hyperelastic parameter, r_1 (Å)	10.50	18.20
Fracture parameter, r_{fracture} (Å)	13.20	21.00
Equilibrium angle, θ_0 (degrees)	180.00	180.00
Tensile stiffness parameter, k_θ (kcal/mol/ rad^2)	14300.00	15.00
LJ parameter, ε (kcal/mol)	15.10	10.6
LJ parameter, σ (Å)	9.35	14.72

Source: Buehler, M. J., *J. Mater. Res*., 21(11), 2855–2869, 2006; Buehler, M. J., *J. Mech. Behav. Biomed. Mater*., 1(1), 59–67, 2008.

Note: Derived from atomistic modeling and corresponding to Equations 3.23, 3.30, 3.34, and 3.38, as well as Section 3.3.1 (units in brackets).

atomistic simulations and the formulation described herein, specifically Equations 3.6, 3.13, 3.17, and 3.21.

It is noted that in the case of tropocollagen, which is typically found in solution, the influence of the solvent on the behavior of the macromolecules is captured in the aforementioned model constants, such that no explicit modeling of solvent is required. Typically, such models do not require an explicit solvent nor an implicit solvent force field or frictional coefficient. The effect of solvation is captured implicitly by the derived parameters and integrated into the coarse-grain potentials.

3.2.2 Model Applications

3.2.2.1 Application 1: Self-Folding of Large Aspect Ratio Carbon Nanotubes and Nanotube Bundles

Large aspect ratio CNTs are extremely flexible and can be deformed into almost arbitrary shapes with relatively small energetical effort [1]. As illustrated by the development of the coarse-grain pair potential, different adjacent CNTs attract each other via van der Waals forces. If different parts of the same tube come sufficiently close, these attractive forces can initiate the formation of self-folded structures, where adjacent tube sections align, forming a racket-like structure. Such structures have been observed in MD simulations [18] as well as experimentally [19]. The stability, self-assembly, and mechanical properties of these structures are difficult to probe experimentally, and become computationally expensive for full atomistic simulations as the length of required nanotube increases. The described coarse-grain model was implemented to investigate the stability of folded structures, as well as the variation of folded configurations as a function of adhesion strength. Further, coarse-grain nanotubes were simulated in bundled configurations (up to 100 nanotubes per bundle) to determine mechanical properties and behavior under compressive, tensile, and bending deformations (see Figure 3.6).

The simple mesoscale model developed can easily be adapted for different types of carbon nanotubes, and allows the direct simulation of hierarchical bundled structures. Such investigations can potentially be of use for the development of carbon-nanotube-reinforced nanocomposites that attempt to utilize the adhesion properties

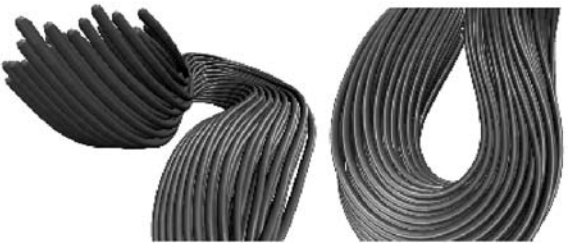

FIGURE 3.6 Simulation snapshot of response of a CNT bundle under mechanical compressive loading depicting significantly deformed/buckled shape. The bundle consists of 81 nanotubes using coarse-grain representation. (From Buehler, M.J., *J. Mater. Res.* 21(11), 2855–2869, 2006. With permission.)

of nanotube clusters and exploit energetically favorable folded configurations and manipulate stable adhesion domains.

3.2.2.2 Application 2: Mechanical and Surface Properties of Vertically Aligned CNT Arrays

Synthesis techniques have become adept at producing arrays of carbon nanotubes consisting of thousands of aligned tubes with similar diameters, lengths, and aspect ratios [2,20]. The properties of such arrays can be exploited to produce novel materials with unique, amplified, and controlled mechanical properties. Again, it is difficult to simulate such systems via full atomistic representations due to the sheer number of required nanotubes and timescales required to mimic real physical and experimental processes.

A vertically aligned array of nanotubes was constructed using the discussed coarse-grain CNT model, and then subjected to nanoindentation simulations (Figure 3.7). The goal was to probe the global behavior and mechanical properties of the array, through variations in nanotube parameters and application of external forces (in the form of a magnetic field). We again stress the use of a coarse-graining approach to investigate the system-level response of the array as opposed to the constituent nanotubes (component-level).

The coarse-grain model inherently allows the efficient varying of array geometry (aspect ratios, array spacing, etc.) to investigate behavior dependencies and pattern formation. Combined with a representation of physical experimental techniques (nanoindentation) to derive physical properties, such models can serve to facilitate empirical investigations by providing efficient means of prediction and a theoretical basis for behavior, thereby providing a crucial link between simulation and reality.

3.2.2.3 Application 3: Mechanical Property Variation through Collagen Fibril Crosslink Density

Natural collagen-based tissues are composed of staggered arrays of ultralong tropocollagen molecules extending to several hundred nanometers [4]. Although the macroscopic properties of collagen-based tissues (such as bone and tendon) have

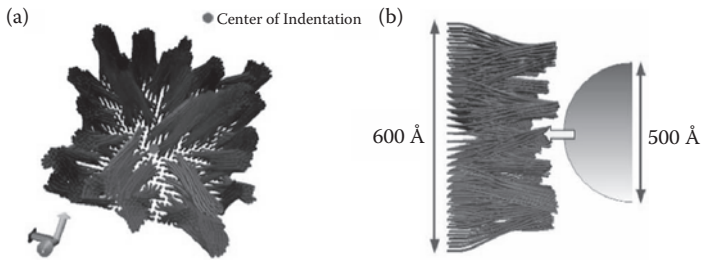

FIGURE 3.7 Depiction of nanoindentation simulation of coarse-grain nanotube array consisting of a 30 × 30 grid of nanotubes with a height of 30.0 nm [2]. (a) Top view, indenter not shown. (b) Side view with relative size of indenter depicted. The coarse-grain simulation consists of approximately 30,000 beads, whereas the equivalent full atomistic representation of the system would consist of over 4 million carbon atoms.

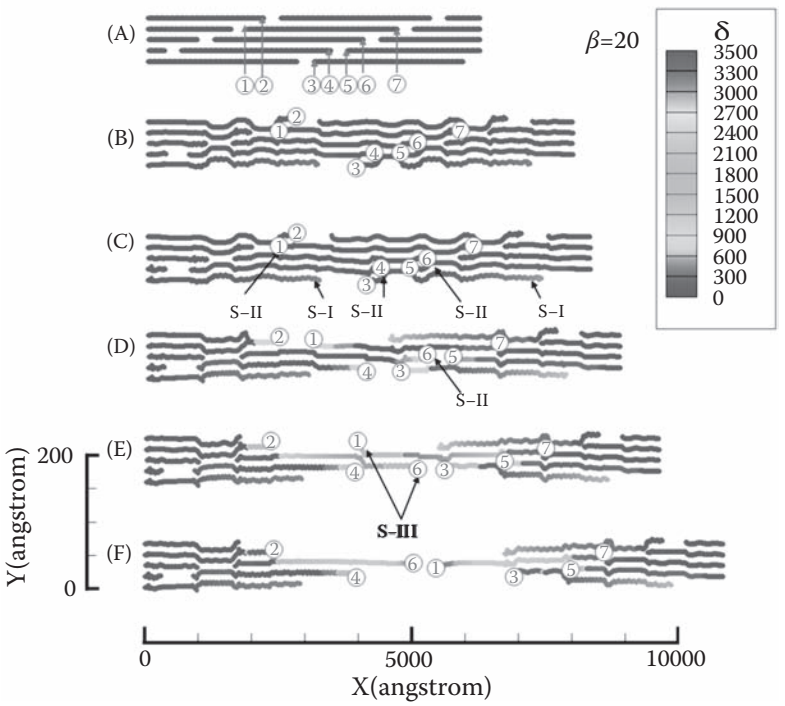

FIGURE 3.8 **(See color insert following page 146.)** Mesoscale model of collagen fibril, consisting of a two-dimensional array of ultralong coarse-grain tropocollagen molecules. The snapshots show the molecular structure as the fibril undergoes tensile deformation, where the color is defined by the magnitude of the slip vector [61]. A detailed analysis of the molecular deformation mechanisms suggests that intermolecular slip plays a major role in mediating large tensile strains in collagen fibrils leading up to failure, following a significant elastic regime. (Adapted from Tang, Y., Ballarini, R., Buehler, M. J., and Eppell, S. J., *J. Roy. Soc. Interface*, 7(46), 839, 2010.)

been studied extensively, less is known about the nanomechanical properties at the mesoscale—the hierarchical structure formed by the staggered tropocollagen molecules. A coarse-grain representation is uniquely suited to investigate the behavior of the structure and interaction of collagen fibrils. One such investigation probed the effect of crosslink density on the mechanical strength, deformation, yield, and fracture behavior on collagen fibrils (Figure 3.8). Crosslink-deficient collagen fibrils show a highly dissipative deformation behavior with large yield regimes, while increasing crosslink densities leads to stronger fibrils that display increasingly brittle behavior.

Collagen is such a fundamental constituent of biological materials that an improved understanding of the relevant nanomechanics can facilitate the development of novel biomimetic materials and aid in the understanding of injury and pathology processes. Indeed, the mutable collagenous tissue of echinoderms serves as an inspiration of new pharmacological agents and composite materials with biomedical applications [21]. In addition, diseases such as *osteogenesis imperfecta* [22]

are caused by defects in the molecular structure of collagen, altering the intermolecular and molecular properties due to genetic mutations [23–26]. Investigations of the effects of such mutations on the subsequent mechanical behavior and properties of collagen structures can serve to elucidate the characterization and diagnosis of diseased tissues and the pathology of similar genetic diseases [27,28]. Such investigations are only possible via multiscale coarse-graining approaches that transcend the hierarchy of collagen fibrils, from the constituent polypeptides to tropocollagen molecules to collagen fibrils, penultimately leading to a deeper understanding of biological tissues such as nascent bone and associated disease states.

3.3 CASE STUDY II: FOLDING/UNFOLDING OF ALPHA-HELICAL PROTEIN DOMAINS

Proteins constitute the critical building blocks of life, providing essential mechanical functions to biological systems, and the focus of many molecular and atomistic level simulations [29,30]. In particular, alpha-helical (AH) protein domains are the key constituents in a variety of biological materials, including cells, hair, hooves, and wool. While continuum mechanical theories have been very successful coupling the atomistic and macro scales for crystalline materials, biological materials and soft condensed matter (such as polymer composites) require different approaches to describe elasticity, strength, and failure. The fundamental deformation and failure mechanisms of biological protein materials remain largely unknown due to a lack of understanding of how individual protein building blocks respond to mechanical load.

It has been determined both experimentally [31] and via simulation [32] that the mechanical response of biological materials is a combination of molecular unfolding or sliding, with a particular significance of rupture of reversible chemical bonds such as hydrogen bonds (H-bonds), covalent crosslinks, or intermolecular entanglement. The dominance of specific mechanisms can emerge at different time and length scales, chemical environments of the protein, and hierarchical arrangements/structures. As such, it is difficult to generalize fully atomistic results from nano to macro. Figure 3.9 displays an example hierarchical alpha-helical protein system.

A coarse-grain model is developed here to investigate the unfolding behavior of alpha-helical domains. The coarse-grain representation integrates parameters that define the energy landscape of the strength properties of alpha-helical protein domains, including energy barriers, unfolding and refolding distances, and the location of folded and unfolded states, and is implemented to investigate the variations of strength with respect to length and loading rate of alpha-helical protein filaments. Although unfolding of short alpha-helical segments can be modeled using full atomistic techniques, a coarse-grain representation is required to fully investigate the length dependence on mechanical response, as well as integration of alpha-helices into higher-level hierarchical arrangements. Such an approach intends to extend a known atomistic behavior to larger systems via coarse-grain potentials, which differs from the intent of the aforementioned carbon nanotube or collagen models that focused on system-level behavior and mechanical response.

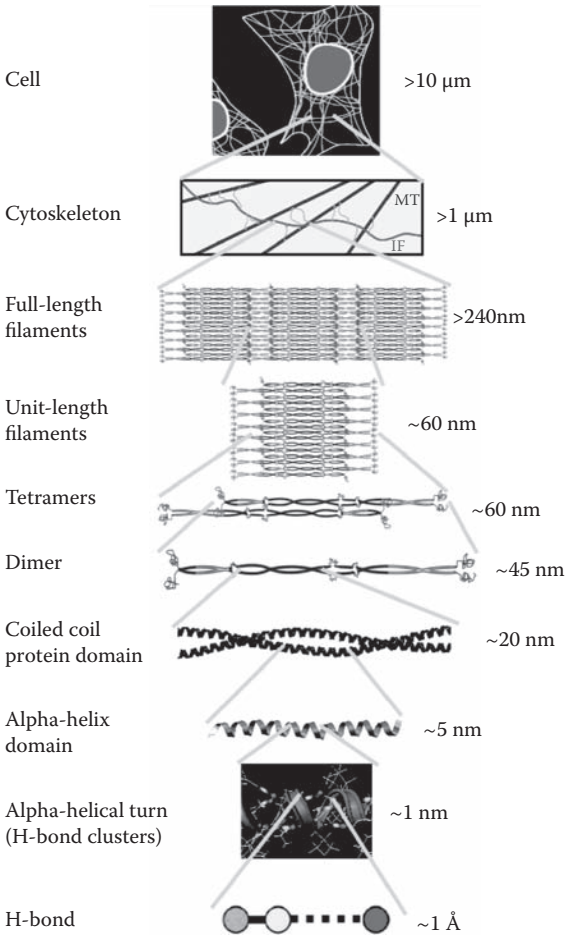

FIGURE 3.9 (See color insert following page 146.) Schematic depicting hierarchical structure of alpha-helix protein-based intermediate filaments (IFs), which provide structural tensegrity to the cytoskeleton of cellular membranes. Over seven levels of hierarchy are transcended, from hydrogen bonds to alpha-helical turns, alpha-helical proteins (which are the focus of coarse-graining discussed here), dimers (coiled-coiled protein domain), tetramers, unit-length filaments, and full-length filaments to the cellular level. (Adapted from Qin, Z., Kreplak, L., and Buehler, M.J., *PLos ONE*, 4(10), e7294, 2009.)

3.3.1 Model Development

The setup of the coarse-grain model for alpha-helical protein domains is based on the geometry of an AH, which features a linear array of turns or convolutions stabilized through the presence of H-bonds between sequential amino acid residues. During mechanical loading, any one of these convolutions can possibly rupture. As such, the coarse-grain representation is rationally discretized into bead-spring elements representing a single convolution consisting of approximately 3.6 amino acid

residues. To achieve the coarse-grained description, the entire sequence of amino acids that constitute the alpha-helices is replaced by a collection of mesoscopic bead-spring elements (see Figure 3.10).

Similar to the previous linear, one-dimensional bead-spring models, we define the energy landscape of the coarse-grain system by three potentials:

$$E_{\mathrm{AH}} = E_{\mathrm{bond}} + E_{\mathrm{angle}} + E_{\mathrm{pair}} \tag{3.22}$$

Here, the bond potential must represent the structural backbone protein domain, and also the energetic features of the stabilizing H-bonds. The aim is to capture the structural and energetic features of an alpha-helical protein domain. A double-well potential is chosen to capture the existence of two equilibrium states for a convolution, folded and unfolded (see Figure 3.11). The model does not involve explicit solvent; rather, the effect of the solvent on the breaking dynamics of alpha-helical convolutions is captured by an effective double-well potential, parameterized by full atomistic simulations that implemented explicit solvent.

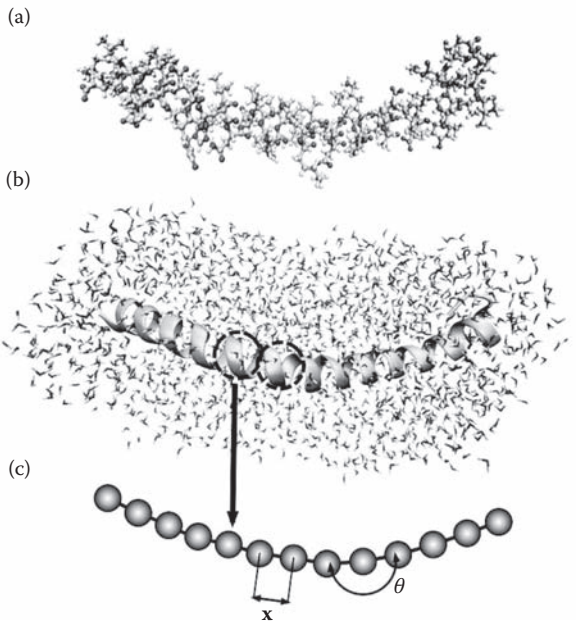

FIGURE 3.10 (See color insert following page 146.) Schematic of coarse-graining procedure, in which full atomistic representation is replaced by a mesoscopic bead-spring model. A pair of beads represents one turn in the alpha-helix (also called a convolution), and thus 3.6 residues with the corresponding mass. (a) Full atomistic representation depicting all atoms and bonds; folded states of the turns are stabilized by the presence of hydrogen bonds between residues (not shown); water molecules not shown for clarity. (b) Ribbon representation of protein, illustrating alpha-helical folded conformation of backbone chain and individual convolutions; explicit solvent (water molecules) shown. (c) Developed coarse-grain representation, with a single bead per convolution; need for explicit solvent eliminated in coarse-grain model, as effects are integrated into coarse-grain potentials.

The bond potential can describe the microscopic details of the rupture mechanism of the convolution H-bonds under force, as well as the transition from a folded to unfolded state, through the prescribed energy barrier of the potential. The description is sufficiently coarse to enable significant computational speedup and efficiency compared with a full atomistic description.

Again, the total bond energy of the alpha-helical system is given by the sum over all bonded interactions or:

$$E_{\text{bond}} = \sum_{\text{bonds}} \phi_{\text{bond}}(x) \tag{3.23}$$

The double-well potential, $\phi_{\text{bond}}(x)$, is given by

$$\phi_{\text{bond}}(x) = \begin{cases} \dfrac{E_b}{x_b^4}\left(x - x_{tr}\right)^2 \left(x - x_{tr} - \sqrt{2}\cdot x_b\right)\left(x - x_{tr} + \sqrt{2}\cdot x_b\right), & x < x_{tr} \\ \dfrac{E_r}{x_r^4}\left(x - x_{tr}\right)^2 \left(x - x_{tr} - \sqrt{2}\cdot x_r\right)\left(x - x_{tr} + \sqrt{2}\cdot x_r\right), & x \geq x_{tr} \end{cases} \tag{3.24}$$

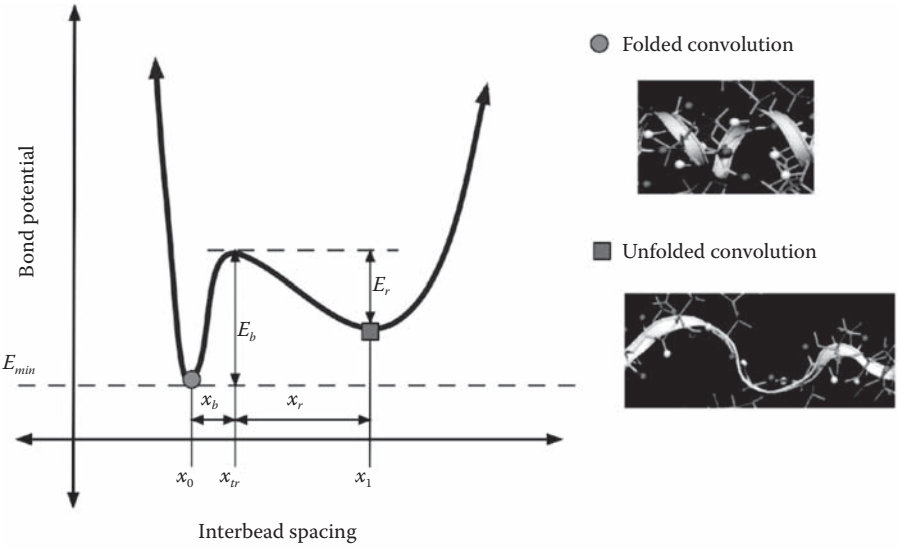

FIGURE 3.11 **(See color insert following page 146.)** Double-well profile of the bond-stretching potential of the coarse-grain model, representing the energy landscape associated with the unfolding of one convolution (see Equation 3.24). The values of the equilibrium states, x_0 and x_1, energy barriers, E_b and E_r, and the transition state, x_{tr}, are obtained from geometric analysis of the alpha-helix geometry, as well as the full atomistic simulations. The transition state (local energy peak) corresponds to the breaking of hydrogen bonds between convolutions of the alpha-helix. After failure of these weak bonds, the convolution unfolds to a second equilibrium state with a large interparticle distance. Under further loading, the covalent bonds begin to stretch, which leads to a second increase of the potential at large deformation.

The first equilibrium reaction coordinate, x_0 (first potential minimum), corresponds to the folded state of one alpha-helical convolution under no force applied. The transition state (energy barrier E_b), with position x_{tr} (peak of potential between the two wells), corresponds to the breaking of the H-bonds between alpha-helical convolutions. After failure of these weak bonds, the alpha-helix unfolds to a second equilibrium state. This corresponds to the second potential minimum with a larger interbead distance, x_1. Under further loading, the backbone bonds begin to be stretched, leading to a second increase in the potential (see Figure 3.11). This formulation does not include the rupture of the covalent backbone bonds. The parameters x_b and E_b represent the distance and energy barrier required to unfold one convolution, which x_r and E_r correspond to the refolding process. It is noted that the energy barrier for refolding, E_r, must be smaller than the energy barrier for unfolding, E_b, since the folded state is the most favorable state for a convolution in equilibrium [33].

The representation of two equilibrium states also requires a transition of the bending stiffness from a folded to unfolded state. In order to distinguish the bending stiffness for each state (which entails a severe structural change), we define a stiffness parameter, K_b, as a function of bead distance, x:

$$K_b(x) = K_{b,\text{fold}}\left[\alpha - \frac{(1-\alpha)}{\pi}\left(\arctan\left(100\left(x - x_{tr}\right)\right) - \frac{\pi}{2}\right)\right], \tag{3.25}$$

with

$$\alpha = \frac{K_{b,\text{unfold}}}{K_{b,\text{fold}}} \tag{3.26}$$

From full atomistic simulations, the bending stiffness of the protein, EI, is determined. We let

$$K_{b,\text{fold}} = \frac{3EI_{\text{fold}}}{x_0} \text{ and } K_{b,\text{unfold}} = \frac{3EI_{\text{unfold}}}{x_1}, \tag{3.27}$$

where EI_{fold} and EI_{unfold} are the bending stiffnesses of the folded and unfolded AH, respectively. Again, the total bending energy of the alpha-helical system is given by the sum over all bead triples (angles), or:

$$E_{\text{angle}} = \sum_{\text{triples}} \phi_{\text{angle}}(x,\theta) \tag{3.28}$$

We can then define the coarse-grain angle potential as

$$\phi_{\text{angle}}(x,\theta) = \frac{1}{2}K_b(x)\left(\theta - \theta_0\right) \tag{3.29}$$

Finally, the total intermolecular interaction energy, E_{pair}, is again represented by the sum over pairwise interactions between beads of different alpha-helical protein

TABLE 3.2
Summary of Parameters for a Coarse-Grain Alpha-Helical Protein Model

Parameter	Numerical Value
Equilibrium distance, folded state, x_0 (Å)	5.4
Equilibrium distance, unfolded state, x_1 (Å)	10.8
Distance between folded state and transition state, x_b (Å)	1.2
Energy barrier, folded state and transition state, E_b (kcal/mol)	11.1
Energy barrier, unfolded state and transition state, E_r (kcal/mol)	6.7
Bending stiffness, folded state, $K_{b,\text{fold}}$ (kcal/mol/rad^2)	21.6
Bending stiffness, unfolded state, $K_{b,\text{unfold}}$ (kcal/mol/rad^2)	0.665
Equilibrium angle, θ_0 (degrees)	180
Pair potential, LJ distance parameter, σ (Å)	10.8
Pair potential, LJ energy parameter, ε (kcal/mol)	6.815
Mass of mesoscale bead (amu)	400

Source: Bertaud, J., et al., J. Phys. Condens. Matter, 2009.

Note: Derived from atomistic modeling, corresponding to Figure 3.12 and representing the constants required for the coarse-grain potentials as discussed in Section 3.3.1 and Equations 3.22 through 3.29 (units in brackets).

domains. The adhesion potential (ϕ_{pair}) is again formulated by a LJ 12:6 potential, via an energy minimum (ε) and distance parameter (σ), in a manner discussed in Section 3.2.1. Table 3.2 lists the parameters implemented in the mesoscopic bead-spring alpha-helix model, from previous full atomistic simulations [29,32,34] depicted in Figure 3.12. The mass of each bead corresponds to the approximate average mass of each convolution (400 amu).

It is quite apparent that, although a similar double-well potential can be developed for other systems with distinct equilibrium conformations, the current coarse-grain description is uniquely developed for the alpha-helix. Specifically, it represents the atomistic rupture behavior of alpha-helical protein domains during mechanical loading under a limited range of loading rates (pulling speeds under 0.3 m/s) at a specific temperature (300 K) and particular environmental conditions (explicit waterbox) implemented in the full atomistic simulations in which the distance and energy barrier parameters were obtained [32,34]. However, the model could be easily adapted to other classes of protein filaments that feature serial arranged domains that undergo unfolding or a transition to distinct equilibrium states under mechanical loading and strain.

3.3.2 Model Applications

3.3.2.1 Application 1: Time Scale Extension

The developed coarse-grain model for the alpha-helix was implemented to investigate the length and rate dependence of the Bell model, a theoretical strength model that can be applied to describe the mechanical behavior of molecules with reversible

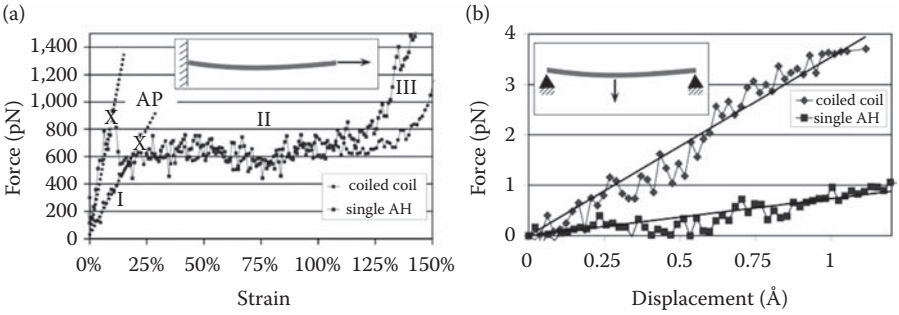

FIGURE 3.12 **(See color insert following page 146.)** Full atomistic tests of alpha-helical protein (single-helix and coiled-coiled conformations) used to parameterize the coarse-grain model. (a) Force-strain results of direct tension simulations. The first regime (I) consists of a linear increase in force, until a strain of approximately 13% for the single alpha-helix, noted as the angular point (AP), which corresponds to the rupture and unfolding of an alpha-helix convolution. The second regime (II) represents the unfolding of the helix under approximately constant force. The third regime represents a nonlinear increase in strain due to backbone stretching of the protein. (b) Force-displacement results of three-point bending simulations. The slope of the curve is proportional to the bending stiffness. Only the single alpha-helix values were used in the development of the coarse-grain representation. (Adapted from Ackbarow, T., and Buehler, M.J., *J. Mater. Sci*., 42(21), 8771–8787, 2007.)

bonds (see Bell [35], Evans [36], Evans and Ritchie [37], and Walton, Lee, and Van Vliet [38], in addition to the primary references, Bertaud et al. [29,30], for details). Essentially, the Bell model presents a logarithmic relationship between reversible bond strength and loading rate (or molecule pulling speed). Full atomistic simulations are limited to time scales on the order of nanoseconds, limiting the pulling of alpha-helix stretching to approximately 0.01 m/s. Such a relatively high loading rate prevents a one-to-one correspondence with experimental results. However, the use of the coarse-grain potential extends the accessible time-scales to an order of microseconds, allowing pulling speeds on the order of 0.0001 m/s, representing a 100-fold increase in time scale. Experimental results of stretching and breaking single AH domains [39,40] report forces corresponding to the force level predictions at ultraslow pulling speeds of the coarse-grain model. Additionally, the coarse-grain representation can still be implemented at time scales on the order of full atomistic studies, allowing the validation of mesoscopic and full atomistic results.

3.3.2.2 Application 2: Length Dependence

The model was further implemented to investigate the length dependence on the rupture strength of proteins to extend the Bell model to ultralong protein regimes. Both experimental and full atomistic investigations are limited to an alpha-helix length on the order of 10 nm. This limitation only represents approximately 20 bead-spring elements of the coarse-grain representation, and thus can be easily surmounted using the coarse-grain model. Extending the length of AH protein domains

to approximately 50 nm, coarse-grain simulations resulted in a logarithmic decrease in rupture strength as the protein length increased or

$$f(L) = a \ln(L/L_0) + b \tag{3.30}$$

Due to the logarithmic dependence on length, this relation can only be investigated by simulating proteins with lengths extending several orders of magnitude. Such an expanse of scales is not accessible to full atomistic representations. This weakening behavior can be attributed to an increase in potential H-bond locations as the number of convolutions increases, each of which can break with the same probability. Since failure of one convolution is sufficient to initiate failure of the entire system, we expect longer molecules to be weaker, as observed in the coarse-grain simulations and previous investigations [41].

3.3.2.3 Application 3: Characterizing Intermediate Filament Networks

Individual, isolated alpha-helices are rarely found in biology. Thus, the developed coarse-grain model can facilitate the investigation of hierarchical structures of proteins and protein filaments [42]. Indeed, AH-based protein networks constitute the

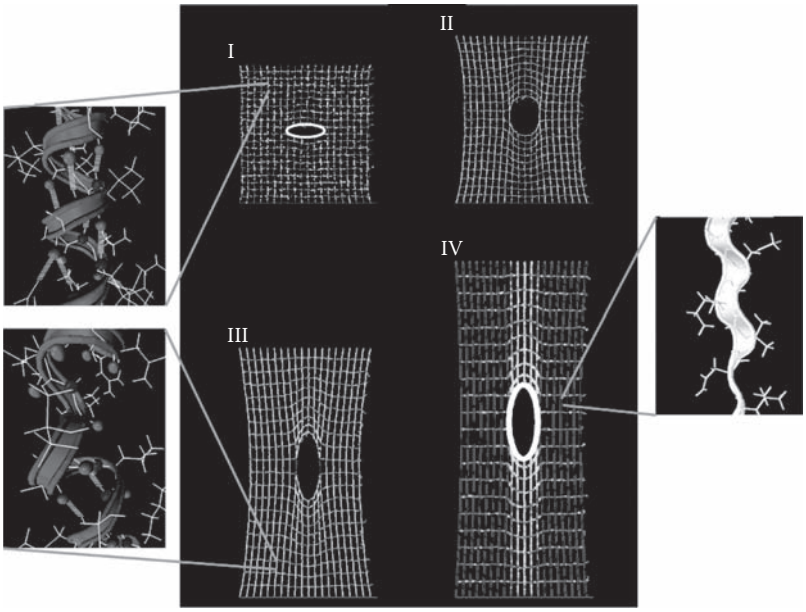

FIGURE 3.13 **(See color insert following page 146.)** Snapshots of protein network deformation, where coarse-grain representation of alpha-helix proteins was implemented. The deformation mechanism is characterized by the molecular unfolding of the alpha-helical protein domains, leading to the formation of large plastic yield regions, providing energy dissipation and preventing catastrophic failure. The blowups depict the atomistic structural arrangement of the alpha-helical protein domains based on the known correspondence with the coarse-grain mapping. (Adapted from Ackbarow, T., et al., *PLos ONE*, 4(6), e6015, 2009.)

intermediate filament structure in the cell's cytoskeleton and the nuclear membrane. Using a network of coarse-grain bead-spring structures, large meshes reflecting an assembly of intermediate filaments can be constructed and probed for mechanical properties and behavior (Figure 3.13).

It was found that the characteristic properties of alpha-helix-based protein networks are due to the particular nanomechanical properties of the protein constituents, enabling the formation of large dissipative yield regions around structural flaws, effectively protecting the protein network against catastrophic failure. The direct simulation of such large networks is only possible through the use of such multiscale coarse-grain models under discussion.

3.4 CASE STUDY III: MESOSCOPIC AGGREGATION OF FULLERENE-POLYMER CLUSTERS

Modification of nanoparticles by attachment of polymer chains can, in principle, allow manipulation of the geometry and interaction of particles on the nanoscale, allowing a tunable method of controlling their self-association [43,44]. A complete understanding of such interactions can result in unique binding properties or controlled self-assembly. Simulations implementing coarse-grain models have shown that nanoparticles tethered by polymer chains with various degrees of asymmetry, chain length, and polymer/particle interaction exhibit a rich spectrum of nanostuctures, including spherical, cylindrical, lamellar, sheetlike, and bicontinuous morphologies [45]. Experimental observations also show self-assembly of such tethered nanoparticles into spherical vesicles [46] and nanorods [47]. Here we focus on poly(ethylene oxide) (PEO)-grafted fullerenes (C_{60}-PEO nanoparticles). The thermodynamics of self-assembly of these nanoparticles, including the strong dependence of cluster distribution and average cluster size on concentration, indicate that the self-assembly process resembles the formation of wormy or spherical micelles, taking advantage of the water-soluble PEO and the hydrophobic fullerene.

Investigation of the formation and aggregation of such nanostructures is limited using full atomistic approaches, as there is a significantly large computational expense to compute the interactions of the nanoparticle (such as the carbon–carbon interactions of the fullerene) and the behavior of the polymer–nanoparticle interactions. Such computations are inconsequential, as it is known *a priori* that the mesoscopic structure is stable. Thus, coarse-graining methods are developed to investigate the subsequent hierarchical level of nanoparticle interactions and aggregation, circumventing the details of full atomistic behavior.

The coarse-graining approach to such systems has a threefold purpose:

1. To reduce the number of degrees of freedom to be simulated
2. To focus on the nanoparticle–nanoparticle interactions
3. To reproduce the molecular distributions and aggregations of the nanoparticles

Specifically, the goal of the coarse-grain model is to adequately reproduce the intramolecular and intermolecular structure of aqueous C_{60}-PEO systems, the

distribution of PEO segments around the fullerenes, and the energetic landscape between nanoparticles.

It is noted that the intended mesoscopic investigation is not focused on mechanical behavior, and thus mechanical properties such as Young's modulus and bending stiffness, critical parameters in the previous potentials (Sections 3.2 and 3.3), are not part of the current coarse-grain model development. However, the C_{60}-PEO coarse-grain system provides an illustration of both the finer-trains-coarser multiscale paradigm, as well as the system-dependent approach to coarse-grain model development expressed throughout this chapter.

3.4.1 Model Development

The coarse-grain model is parameterized based on fullerene–fullerene, fullerene–PEO, and PEO–PEO interactions. Of critical concern, as the nanoparticles aggregate in solution, is the integration of the influence of water on all interactions. Indeed, elimination of the explicit solvent results in the primary reduction of degrees of freedom. Fullerenes were condensed to a single-particle representation, while PEO chains were developed consisting of one particle per CH_2–O–CH_2 functional group (Figure 3.14). The coarse-graining approach for polymer systems is unique in the fact that polymer systems are typically governed by entropic effects (as opposed to the rigid structures of CNTs or tropocollagen). As such, the coarse-grain model focuses on interactions and molecular distributions rather than replication of specific structural or mechanical properties.

We define the energy of the system as

$$E_{\text{PEO-C}_{60}} = E_{\text{pair}}, \tag{3.31}$$

such that

$$E_{\text{PEO-C}_{60}} = \sum_{\text{pair}} \phi_{\text{pair}} \tag{3.32}$$

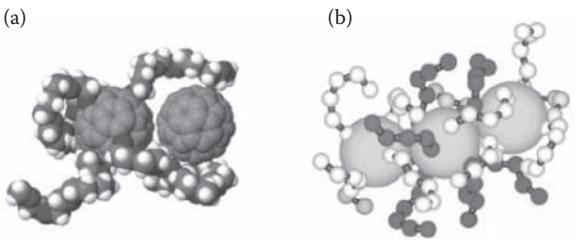

FIGURE 3.14 Representative snapshots of (a) two interacting C_{60}–PEO nanoparticles obtained from atomistic, explicit solvent simulations (water molecules and PEO chains on the right fullerene omitted for clarity) and (b) three coarse-grain C_{60}–PEO nanoparticle representations (PEO beads of the center nanoparticle shaded differently to differentiate adjacent molecules). (Reprinted with permission from Bedrov, D., Smith, G. D., and Li, L., *Langmuir*, 21, 5251–5255, 2005. Copyright 2005 American Chemical Society.)

Here, the coarse-grain potential is defined by the interactions alone. To account for bonding and angular geometry, the SHAKE algorithm was implemented [48] (which applies bond and angle constraints). As the intent of the coarse-grain model is not the mechanical behavior of the nanoparticles, less emphasis is placed on the accurate representation of molecular deformation, and application of the SHAKE algorithm is sufficient to maintain accurate geometry and polymer tether response during aggregation. Each interaction pair was investigated at the atomistic level separately, and can subsequently be considered part of the discussed atomistic test suite, with a focus on molecular interactions rather than molecular mechanical response. Atomistic investigations include

1. PEO–PEO and PEO–water intermolecular and PEO–PEO intramolecular interactions representing both hydrophilic and hydrophobic ether–water interactions [49]
2. Fullerene–fullerene interactions using full atomistic carbon–carbon potential to develop a coarse-grain C_{60}–C_{60} pair potential [50]
3. Water–carbon interactions [51] as the basis for water–fullerene interactions [52]

It is noted that each investigation focused on a particular molecular interaction, similar to previous case studies in which the atomistic test suites focused on individual molecular responses, such as stretching, bending, or adhesion. The interactions were then defined by

$$\phi_{\text{pair}} = \phi_{AB}, \tag{3.33}$$

where ϕ_{pair} is derived from the atomistic test suite. The AB indices indicate the possible fullerene–fullerene, PEO–PEO, or PEO–fullerene interactions. As the atomistic studies did not determine all possible combinatorial parameters, standard mixing rules were implemented:

$$\varepsilon_{AB} = \sqrt{\varepsilon_A \varepsilon_B} \tag{3.34}$$

$$\sigma_{AB} = \frac{1}{2}\left(\sigma_A + \sigma_B\right) \tag{3.35}$$

Using the known atomistic interactions as well as the mixing rules, behavior was investigated between C_{60}–PEO nanoparticles in full atomistic and coarse-grain simulations. Nonbonded coarse-grain PEO–PEO interactions were parameterized to reproduce the PEO monomer–monomer interactions. Bonds and bends in the PEO chains were developed to match intramolecular correlations (end-to-end distance and radius of gyration). Parameterization of the coarse-grain potentials was then adjusted to reflect accurate radial distribution functions and coordination number of

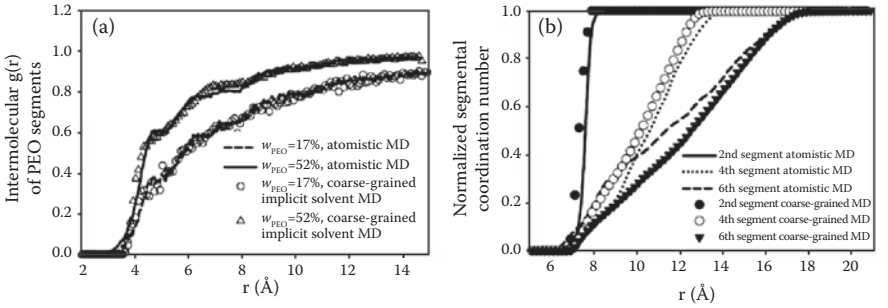

FIGURE 3.15 Full atomistic and coarse-grain results for model parameterization and validation for C_{60}–PEO nanoparticles. (a) PEO–PEO monomer intermolecular radial distribution function as obtained from atomistic, explicit solvent and coarse-grained, implicit solvent MD simulations of two PEO aqueous solutions. (b) Integrated coordination number of PEO segments in the C_{60}–PEO in an aqueous solution system as a function of their separation from the center of fullerene. (Reprinted with permission from Bedrov, D., Smith, G. D., and Li, L., *Langmuir*, 21, 5251–5255, 2005. Copyright 2005 American Chemical Society.)

the C_{60}–PEO system, i.e., the distribution of the polymer tethers about the fullerene (Figure 3.15).

Validation was carried out by calculation of the potential of mean force between two C_{60}–PEO nanoparticles via full atomistic (explicit solvent) and coarse-grain (implicit solvent) simulations. The coarse-grain model captures the most important features of the PMF, namely, the weak long-range attraction and strong short-range attraction. Again, we see how full atomistic investigations are applied to validate the behavior of a system component (as described in Section 2.3.5), after which the coarse-grain model can be extended to investigate larger systems.

3.4.2 Model Applications

3.4.2.1 Application 1: Large Systems of Aqueous C_{60}–PEO Nanoparticles

The coarse-grain representation was implemented to compare the aggregation of 1000 bare fullerene or 1000 C_{60}–PEO nanoparticles in solution, with fullerene volume fractions ranging from 0.07 to 0.25 [43]. Full atomistic simulation of such systems would expend the majority of computational cost on the explicit solvent calculations, consisting of thousands of water molecules with negligible interactions with the nanoparticles, yet a large system is required to investigate the spatial and density effects of nanoparticle aggregation. It was shown that bare fullerenes form dense clusters with interactions between many fullerene neighbors, while the introduction of PEO tethers results in a polymer "hugging" phenomena (coverage of adjacent fullerenes by PEO chains). With an increase in surface coverage, the steric interactions between PEO chains and between PEO and fullerenes become dominant and shield the fullerene from interactions with other fullerenes, resulting in chain-like cluster configurations (Figure 3.16).

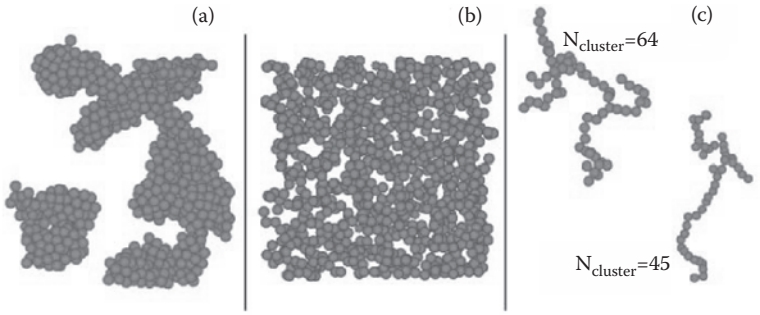

FIGURE 3.16 Representative coarse-grain simulation snapshots of (a) 1000 bare C_{60} fullerenes in aqueous solution (water not shown); (b) 1000 PEO-tethered C_{60} fullerenes, with equivalent volume fraction as (a) (water and PEO chains are not shown for clarity); and (c) two representative PEO–C_{60} clusters from the configuration shown in (b). (Reprinted with permission from Bedrov, D., Smith, G. D., and Li, L., *Langmuir*, 21, 5251–5255, 2005. Copyright 2005 American Chemical Society.)

3.4.2.2 Application 2: Systematic Variation of Polymer Architecture on C_{60}–PEO Nanoparticles

The effect of polymer architecture was investigated using the developed coarse-grain model, by manipulating the number and chain-length of the attached PEO tethers [44]. PEO-grafted fullerenes were comprised of a single tether of 60 repeat units (PEO functional groups), a three-arm star with 20 units per chain, or a six-arm star

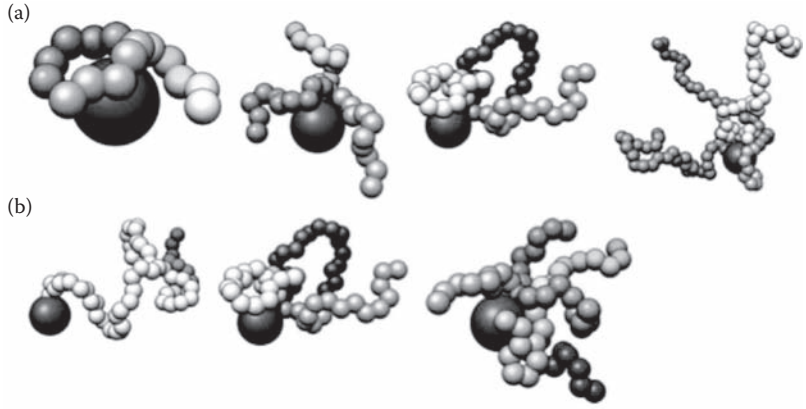

FIGURE 3.17 **(See color insert following page 146.)** Schematic overview of the types of coarse-grain nanoparticles employed in the clustering study. (a) Constant architecture motif, with each chain in a three-armed star with lengths of 5, 10, 20, and 40 PEO units, respectively. (b) Constant mass motif, where each nanoparticle has 60 total PEO units with arrangements in a linear, three-armed, or six-armed fashion, respectively. Note explicit solvent molecules are neither depicted nor required in the coarse-grain simulations. (Reproduced with permission of the PCCP Owner Societies. Copyright 2009. Hooper, J. B., Bedrov, D., and Smith, G. D., *Phys. Chem. Chem. Physics*, 11, 2034–2045, 2009.)

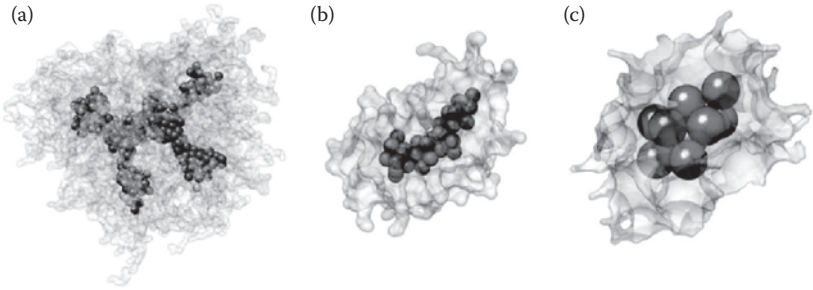

FIGURE 3.18 Representative snapshots for the constant mass series of clusters as depicted in Figure 3.17b: (a) Single, 60-unit PEO chains; (b) three-armed configuration, 20 units each; (c) six-armed configuration, 10 units each. The red spheres represent the fullerene core, while the surrounding polymer is depicted as a solvent-accessible isosurface. (Reproduced in part with permission of the PCCP Owner Societies. Copyright 2009. Hooper, J. B., Bedrov, D., and Smith, G. D., *Phys. Chem. Chem. Physics*, 11, 2034–2045, 2009.)

with 10 units per chain (Figure 3.17b). In addition, the influence of tether length of the three-chain configuration was investigated, from 5 to 40 units per chain (Figure 3.17a). Variation of number of PEO segments and segment length serve to control aggregate size and shape during self assembly.

It was concluded that higher molecular weight PEO (longer arms) and more compact PEO (more arms but constant total number of units) resulted in greater steric repulsion between fullerenes, engendering greater aggregate surface curvature and resulting in more spherically shaped aggregates (Figure 3.18).

It is emphasized that while the coarse-grained simulations were able to eliminate solvent degrees of freedom, the degrees of freedom of the tethered polymer chains cannot be excluded due to the nontrivial and nonisotropic contribution of the functional monomer groups into the interaction between C_{60}-PEO nanoparticles. Again, care must be taken to ensure such pertinent effects are included in any developed coarse-grain representation.

Such studies illustrate that chemical modifications of nanoparticles can result in unexpected interaction/self-assembly behavior due to interplay between nanoscale phenomena—phenomena that may be beyond the scope of atomistic investigations. The understanding of nanoparticle aggregations such as polymer-tethered fullerenes can facilitate the development of complex nanoscale structures with potential biomedical applications (i.e., drug delivery, binding to biological molecules) or advance polymer nanocomposites with superior mechanical properties.

3.5 SUMMARY AND CONCLUSIONS

Model formulation is dependent on the molecular system to be represented, as well as the intent of the coarse-grain simulations. In the model development for carbon nanotubes and tropocollagen molecules, a focus was on structure–property relations of secondary hierarchical structures such as CNT bundles or arrays and collagen fibrils. The intent of the investigation was to probe the mechanics of the larger

hierarchical systems, and care was taken to accurately represent the mechanical response of the coarse-grain potential. Consequently, this lead to the integration of molecular softening and stiffening of carbon nanotubes and tropocollagen molecules within the coarse-grain response. The intention of the coarse-grain representation of alpha-helix protein domains, in contrast, was to extend well-known atomistic behavior to time and length scales inaccessible to full atomistic molecular dynamics. The integration of the unfolding behavior of an alpha-helix reduced the complex phenomena of hydrogen-bond rupture to a simple bond potential, via a unique "double well" potential formulation. In effect, the coarse-grain representation can accurately represent the response of two distinct configurations of the protein—both helical and unfolded—within the same model. For nanoparticle aggregation, the coarse-grain model development concentrated on polymer–nanoparticle interactions, with limited focus on mechanical properties. The intended application is not to produce a mechanical response, but rather to systematically study the effects of nanoparticle concentration and polymer architecture on self-assembly processes. As such, accurate mechanical properties and associated potentials were not required, further optimizing the computational efficiency of the simulations, required atomistic tests, and development of the coarse-grain model.

It is apparent that current coarse-graining methods are neither as accurate nor as predictive as all atom simulations. Future coarse-graining techniques can explore more rigorous parameterization methodologies for more accurate representations of the system. Indeed, full atomistic force fields and algorithms are constantly updated to improve the accuracy of results and versatility of applications. With an inevitable increase in computing power, larger and larger systems can be simulated via full atomistic representations, providing a counterargument for the development of any coarse-graining approaches. In addition, coarse-graining methods are inherently at a disadvantage due to their system-dependent nature—complex and diverse interactions must be described by a small number of parameters. The finer-trains-coarser multiscale paradigm implemented here attempts to illustrate the possible utility and advantages of coarse-graining methods through the delineation of component-level material properties and system-level mechanical behavior. The convergence of structure and mechanical properties is apparent in both natural and synthetic hierarchical systems, requiring new approaches to analyze and explicate the reciprocity of material properties, mechanical function, and structural arrangement. It is the contention of all multiscale methods that component-level behaviors can be adeptly represented by coarse-grain potentials, and thus serve to clarify structure-property relations without resorting to more complex models.

ACKNOWLEDGMENTS

This research was supported by the Army Research Office (W911NF-06-1-0291), by the National Science Foundation, (CAREER Grant CMMI-0642545 and MRSEC DMR-0819762), the Air Force Office of Scientific Research (FA9550-08-1-0321), the Office of Naval Research, (N00014-08-1-00844), and the Defense Advanced Research Projects Agency (DARPA) (HR0011-08-1-0067). M. J. B. acknowledges support through the Esther and Harold E. Edgerton Career Development Professorship.

REFERENCES

1. Buehler, M. J. 2006. Mesoscale modeling of mechanics of carbon nanotubes: Self-assembly, self-folding, and fracture. *Journal of Materials Research* 21(11):2855–2869.
2. Cranford, S. and M. J. Buehler. 2009. Mechanomutable carbon nanotube arrays. *International Journal of Materials and Structural Integrity* 3(2/3):161–178.
3. Buehler, M. J. 2006. Atomistic and continuum modeling of mechanical properties of collagen: Elasticity, fracture, and self-assembly. *Journal of Materials Research* 21(8): 1947–1961.
4. Buehler, M. J. 2008. Nanomechanics of collagen fibrils under varying cross-link densities: Atomistic and continuum studies. *Journal of the Mechanical Behavior of Biomedical Materials* 1(1):59–67.
5. Buehler, M. J. 2007. Molecular nanomechanics of nascent bone: Fibrillar toughening by mineralization. *Nanotechnology* 18:295102.
6. Baughman, R. H., A. A. Zakhidov, and W. A. de Heer. 2002. Carbon nanotubes—the route towards applications. *Science* 297:787–792.
7. Treacy, M. M. J., T. W. Ebbesen, and J. M. Gibson. 1996. Exceptionally high Young's modulus observed for individual carbon nanotubes. *Nature* 381:678–680.
8. Li, F. et al. 2000. Tensile strength of single-walled carbon nanotubes directly measured from their macroscopic ropes. *Applied Physics Letters* 77(20):3161.
9. Bhattacharjee, A. and M. Bansal. 2005. Collagen structure: The Madras triple helix and the current scenario. *IUBMB Life* 57(3):161–172.
10. Gautieri, A., M. J. Buehler, and A. Redaelli. 2009. Deformation rate controls elasticity and unfolding pathway of single tropocollagen molecules. *Journal of the Mechanical Behavior of Biomedical Materials* 2(2):130–137.
11. Sun, Y.-L. et al. 2004. Stretching type II collagen with optical tweezers. *Journal of Biomechanics* 37(11):1665–1669.
12. An, K.-N., Y.-L. Sun, and Z.-P. Luo. 2004. Flexibility of type I collagen and mechanical property of connective tissue. *Biorheology* 41:239–246.
13. Maskarinec, S. A. and D. A. Tirrell. 2005. Protein engineering approaches to biomaterials design. *Current Opinion in Structural Biology* 16:422–426.
14. Lorenzo, A. C. and E. R. Caffarena. 2005. Elastic properties, Young's modulus determination and structural stability of the tropocollagen molecule: A computational study by steered molecular dynamics. *Journal of Biomechanics* 38(7):1527–1533.
15. Buehler, M. J., F. F. Abraham, and H. Gao. Hyperelasticity governs dynamic fracture at critical length scales. *Nature* 426:141–146.
16. Buehler, M. J. and H. Gao. 2006. Dynamical fracture instabilities due to local hyperelasticity at crack tips. *Nature* 439:307–310.
17. Timoshenko, S. and G. H. Maccullough. 1940. *Elements of strength of materials*, 2nd ed. New York: D. Van Nostrand Company, Inc.
18. Buehler, M. J. et al. 2006. Self-folding and unfolding of carbon nanotubes. *Journal of Engineering Materials and Technology* 128:3–10.
19. Cohen, A. E. and L. Mahadevan. 2003. Kinks, rings, and rackets in filamentous structures. *Proceedings of the National Academy of Sciences* 100(21):12141–12146.
20. Qi, H. J. et al. 2003. Determinaton of mechanical properties or carbon nanotubes and vertically aligned carbon nanotube forests using nanoindentation. *Journal of Mechanics and Physics of Solids* 51:2213–2237.
21. Wilkie, I. C. 2005. Mutable collagenous tissue: Overview and biotechnological perspective. In *Echinodermata*, eds. W. E. G. Muller and V. Matranga, 221–250. Berlin–Heidelberg: Springer.
22. Rauch, F. and F. H. Glorieux. 2004. Osteogenesis imperfecta. *Lancet* 363:1377–1385.

23. Sillence, D. O., A. Senn, and D. M. Danks. 1979. Genetic heterogeneity in osteogenesis imperfecta. *Journal of Medical Genetics* 16:101–116.
24. Roughley, P. J., F. Rauch, and F. H. Glorieux. 2003. Osteogenesis imperfecta—clinical and molecular diversity. *European Cells and Materials* 5:41–47.
25. Beck, K. et al. 2000. Destabilization of osteogenesis imperfecta collagen-like model peptides correlates with the identity of the residue replacing glycine. *Proceedings of the National Academy of Sciences* 97(8):4273–4278.
26. Misof, K. et al. 1997. Collagen from the osteogenesis imperfecta mouse model (OIM) shows reduced resistance against tensile stress. *Journal of Clinical Investigation* 100: 40–45.
27. Gautieri, A. et al. 2009. Molecular and mesoscale mechanisms of osteogenesis imperfecta disease in collagen fibrils. *Biophysical Journal* 97:857–865.
28. Gautieri, A. et al. 2009. Single molecule effects of osteogenesis imperfecta mutations in tropocollagen protein domains. *Protein Science* 18:161–168.
29. Bertaud, J., Z. Qin, and M. J. Buehler. 2009. Atomistically informed mesoscale model of alpha-helical protein domains. *International Journal for Multiscale Computational Engineering* 7(3):237–250.
30. Bertaud, J. et al. 2009. Energy landscape, structure and rate effects on strength properties of alpha-helical proteins. *Journal of Physics: Condensed Matter* 22:035102.
31. Dietz, H. et al. 2006. Anisotropic deformation response of single protein molecules. *Proceedings of the National Academy of Sciences* 103(34):12724–12728.
32. Ackbarow, T. et al. 2007. Hierarchies, multiple energy barriers, and robustness govern the fracture mechanics of alpha-helical and beta-sheet protein domains. *Proceedings of the National Academy of Sciences* 104(42):16410–16415.
33. Karcher, H. et al. 2006. A coarse-grained model for force-induced protein deformation and kinetics. *Biophysical Journal* 90(8):2686–2697.
34. Ackbarow, T. and M. J. Buehler. 2007. Superelasticity, energy dissipation and strain hardening of vimentin coiled-coil intermediate filaments: Atomistic and continuum studies. *Journal of Materials Science* 42(21):8771–8787.
35. Bell, G. I. 1978. Models for the specific adhesion of cells to cells. *Science* 200(4342): 618–627.
36. Evans, E. 2001. Probing the relation between force, lifetime, and chemistry in single molecular bonds. *Annual Reviews in Biophysics and Biomolecular Structure* 30(1):105–128.
37. Evans, E. and K. Ritchie. 1997. Dynamic strength of molecular adhesion bonds. *Biophysical Journal* 72:1541–1555.
38. Walton, E. B., S. Lee, and K. J. Van Vliet. 2008. Extending Bell's model: How force transducer stiffness alters measures unbinding forces and kinetics of molecular complexes. *Biophysical Journal* 94:2621–2630.
39. Lantz, M. A. et al. 1999. Stretching the alpha-helix: A direct measure of the hydrogen-bond energy of a single-peptide molecule. *Chemical Physics Letters* 315(1):61–68.
40. Kageshima, M. et al. 2001. Insight into conformational changes of a single alpha-helix peptide molecule through stiffness measurements. *Chemical Physics Letters* 343(1):77–82.
41. Qi, H. J., C. Ortiz, and M. Boyce. 2006. Mechanics of biomacromolecular networks containing folded domains. *Journal of Engineering Materials and Technology* 128(4):509–518.
42. Ackbarow, T. et al. 2009. Alpha-helical protein networks are self-protective and flaw-tolerant. *PLos ONE* 4(6):e6015.
43. Bedrov, D., G. D. Smith, and L. Li. 2005. Molecular dynamics simulation study of the role of evenly spaced poly(ethylene oxide) tethers on the aggregation of C_{60} fullerenes in water. *Langmuir* 21:5251–5255.

44. Hooper, J. B., D. Bedrov, and G. D. Smith. 2009. The influence of polymer architecture on the assembly of poly(ethylene oxide) grafted C_{60} fullerene clusters in aqueous solution: A molecular dynamics simulation study. *Physical Chemistry Chemical Physics* 11:2034–2045.
45. Zhang, Z. et al. 2003. Tethered nano building blocks: Toward a conceptual framework for nanoparticle self-assembly. *Nano Letters* 3(10):1341–1346.
46. Zhou, S. et al. 2001. Spherical bilayer vesicles of fullerene-based surfactants in water: A laser light scattering study. *Science* 291:1944.
47. Sawamura, M. et al. 2002. Stacking of conical molecules with a fullerene apex into polar columns in crystals and liquid crystals. *Nature* 419:702.
48. Ryckaert, J. P., G. Ciccotti, and H. J. C. Berendsen. 1977. Numerical integration of the Cartesian equations of motion of a system with constraints: Molecular dynamics of n-alkanes. *Journal of Computational Physics* 23:327–341.
49. Smith, G. D., O. Borodin, and D. Bedrov. 2002. A revised quantum chemistry-based potential for poly(ethylene oxide) and its oligomers in aqueous solution. *Journal of Computational Chemistry* 23:1480.
50. Girifalco, L. A. 1992. Molecular properties of C_{60} in the gas and solid phases. *Journal of Physical Chemistry* 96(2):858–861.
51. Werder, T. et al. 2003. On the water-carbon interaction for use in molecular dynamics simulations of graphite and carbon nanotubes. *Journal of Physical Chemistry B* 107:1345–1352.
52. Li, L., D. Bedrov, and G. D. Smith. 2005. Repulsive solvent-induced interaction between C_{60} fullerenes in water. *Physical Review E* 71:011502.
53. Pilcher, H. R. 2003. Alzheimer's abnormal brain proteins glow. *Nature News* September 23, 2003.
54. Xu, Z., R. Paparcone, and M. J. Buehler. 2010. Alzheimer's Aβ(1-40) amyloid fibrils feature size dependent mechanical properties. *Biophysical Journal* 98(10):2053–2062.
55. Monticelli, L. et al. 2008. The MARTINI coarse-grained force field: Extension to proteins. *Journal of Chemical Theory and Computation* 4:819–834.
56. Marrink, S. J., A. H. de Vries, and A. E. Mark. 2004. Coarse grained model for semiquantitative lipid simulations. *Journal of Physical Chemistry B* 108:750–760.
57. McClain, D. et al. 2007. Electrostatic shielding in patterned carbon nanotube field emission arrays. *Journal of Physical Chemistry C* 111(20):7514–7520.
58. Yang, J. and L. Dai. 2003. Multicomponent interposed carbon nanotube micropatterns by region-specific contact transfer and self-assembling. *Journal of Physical Chemistry B* 107:12387–12390.
59. Buehler, M. J., S. Keten, and T. Ackbarow. 2008. Theoretical and computational hierarchical nanomechanics of protein materials: Deformation and fracture. *Progress in Materials Science* 53:1101–1241.
60. Qin, Z., L. Kreplak, and M. J. Buehler. 2009. Hierarchical structure controls nanomechanical properties of vimentin intermediate filaments. *PLos ONE* 4(10):e7294.
61. Tang, Y., R. Ballarini, M. J. Buehler, and S. J. Eppell. 2010. Micromechanisms of deformation of collagen fibrils under uniaxial tension. *Journal of the Royal Society, Interface* 7(46), 839.